LETTER

A unified system-level simulation framework for energy harvesting, management, and application in plucking piezoelectric energy harvesters

Letters
IOP Publishing
Smart Materials and Structures
Smart Mater. Struct. **34** (2025) 05LT01 (11pp)
https://doi.org/10.1088/1361-665X/add8d4

Letter

A unified system-level simulation framework for energy harvesting, management, and application in plucking piezoelectric energy harvesters

Hao Tang[1], Xuzhang Peng[1], Xin Li[2], Dewen Yu[3], Yunlong Zi[4] and Guobiao Hu[1,*]

[1] Thrust of Internet of Things, The Hong Kong University of Science and Technology (Guangzhou), Guangzhou, Guangdong 511400, People's Republic of China
[2] Guangzhou Institute of Technology, Xidian University, Guangzhou, Guangdong 510555, People's Republic of China
[3] Frontier Institute of Science and Technology, Xi'an Jiaotong University, Xi'an 710049, People's Republic of China
[4] Thrust of Sustainable Energy and Environment, The Hong Kong University of Science and Technology (Guangzhou), Nansha, Guangzhou 511400, Guangdong, People's Republic of China

E-mail: guobiaohu@hkust-gz.edu.cn

Received 10 January 2025, revised 4 May 2025
Accepted for publication 14 May 2025
Published 21 May 2025

Abstract

Piezoelectric energy harvesting technology empowers systems with self-sustainability for applications in distributed scenarios, such as the Internet of Things (IoT). Although extensively studied, existing studies fail to integrate all essential system units within a unified paradigm for analysis. This study addresses this research gap by developing a comprehensive system-level equivalent circuit model (ECM) that incorporates a transient motion (TM)-driven piezoelectric energy harvester (PEH), a self-powered synchronous electronic charge extraction (SP-SECE) circuit, an energy management unit (LTC3588-1 module), and two distinct types of electronic devices. Within this framework, the ECM can simulate the whole operating process of the TM-PEH, from mechanical excitation through energy conversion & storage to the operation of electronic devices. Experiments were conducted, and the results perfectly aligned with simulation findings. Both simulation and experimental results demonstrated that the SP-SECE circuit increased harvested energy by nearly five times compared to the standard energy harvesting (SEH) circuit when charging a capacitor of 330 μF. This superior energy harvesting capability enables the operation of electronic devices under conditions where the SEH circuit would fail. Moreover, the established system-level model demonstrates its adaptability for simulating both continuous and intermittent load devices. These findings underscore the model's potential for optimizing energy harvesting systems and improving the design of self-powered IoT applications in an unprecedented manner from a holistic perspective.

* Author to whom any correspondence should be addressed.

Keywords: piezoelectric energy harvesting, equivalent circuit model, plucking, energy management, system-level simulation

1. Introduction

The rapid advancement of the Internet of Things (IoT) has provided great convenience to our daily lives [1] and industrial production [2] while increasing the demand for a distributed, eco-friendly energy solution across diverse scenarios [3, 4]. The pressing need for sustainable energy has ushered in the development of efficient and reliable energy supply systems. Mechanical energy ubiquitously exists in the ambient environment, manifesting in activities such as vibrations of roads and bridges, as well as the operation of production lines. Converting mechanical energy into electricity provides a promising solution for scattered energy supply needs of pervasive IoT nodes [5, 6]. Among various energy transduction mechanisms, including piezoelectric [7], electromagnetic [8], and triboelectric [9], piezoelectric transduction has garnered significant attention due to its structural simplicity, high power density, and cost-effectiveness [10].

In the community of piezoelectric energy harvesting, a cantilever beam subjected to steady-state and continuous base excitation is a standard design [11, 12]. However, this design has the limitation of a narrow operational bandwidth [13]. In contrast, the environmental vibrations in real-world scenarios are inherently unpredictable, random, transient, and discontinuous. A slight deviation from the resonant frequency would lead to a drastic reduction in power output, posing significant challenges for the practical applications of piezoelectric energy harvesters (PEHs) [14]. Researchers have proposed a lot of strategies to broaden the operational bandwidth of PEHs, including introducing nonlinearities [5], utilizing self-adaptive structures [15], and employing frequency up-conversion (FUC) mechanisms [16]. Among these methods, beam plucking is an FUC technique well-suited for harvesting energy from ultra-low-frequency vibrations [17–20]. While optimizing the mechanical structure can lead to performance improvements, it is also important to acknowledge that a PEH, being an electromechanical system, has its performance also influenced by the interface circuits [21–23]. Although a standard energy harvesting (SEH) circuit offers the advantage of simplicity, it suffers from an energy backflow issue that limits its efficiency [24]. To address this drawback and boost conversion efficiency, researchers have developed a variety of interface circuits, such as synchronous electric charge extraction (SECE) [25, 26] and synchronized switch harvesting on an inductor (SSHI) circuits [27, 28]. Studies have shown that an advanced interface circuit can help boost efficiency by over several hundred percent. However, traditional methods for analyzing mechanical dynamics and interface circuits are remarkably different. To bridge research in both fields, the equivalent circuit modeling (ECM) method has been developed [29, 30]. This approach allows for incorporating interface circuits, like SECE and SSHI circuits, in the simulation analysis when modeling a PEH.

In addition to interface circuits, from the practical application point of view, an energy management unit (EMU) is crucial to regulate a reliable output voltage for the power end, given the unpredictable nature of ambient excitations. However, previous studies are confined to interface circuit-level simulations [31–33]. This hinders the thorough analysis and optimization of piezoelectric energy harvesting systems towards practical applications. A truly system-level simulation should include the EMU and electronic appliances with complicated nonlinear power characteristics. This study addresses above-mentioned gaps by developing a genuinely system-level ECM and applying it to analyze a TM-PEH. This ECM synthesizes mechanical dynamics, interface circuit features, energy management modules, and sensor operation to enable a comprehensive simulation that connects the theories with practical applications.

2. Mechanical structure overview

Figure 1(a) illustrates the physical prototype of the TM-PEH and the experimental setup for testing. This TM-PEH can be used as a self-powered motion detector [34]. It consists of a piezoelectric cantilever beam with an attached tip magnet (M1) and another driving magnet (M2). The piezoelectric cantilever beam can be mounted on the door frame, and the driving magnet can be installed on the door. As the door opens or closes, the repulsive magnetic force between M1 and M2 causes the beam to bend, thereby storing elastic potential energy into it. After the stored energy reaches a predefined threshold, it will be automatically released and transformed into kinetic energy, resulting in the underdamped vibration of the beam. In this process, the piezoelectric transducer affixed to the beam converts part of the kinetic energy into electrical energy. In the established experimental setup, door movement was emulated using a linear motor (Kollmorgen©, SMD175), which operated at a constant velocity. Figure 1(b) shows the printed circuit board for regulating the AC output from the TM-PEH, which encompasses the SEH/SP-SECE circuit and the EMU (Linear Technology©, LTC3588-1). A SEH circuit converts the AC voltage output from the TM-PEH to DC. Alternatively, an SP-SECE boosts efficiency and achieves AC-DC conversion. Subsequently, an EMU further stores the energy and regulates the output. When the stored energy falls below a certain threshold, the energy management circuit cuts the power supply to the electronic appliance. Once the stored energy reaches the desired threshold, the EMU establishes the supply and activates the operation of the electronic devices [34, 35]: a hygrothermograph and an IoT node (Nordic

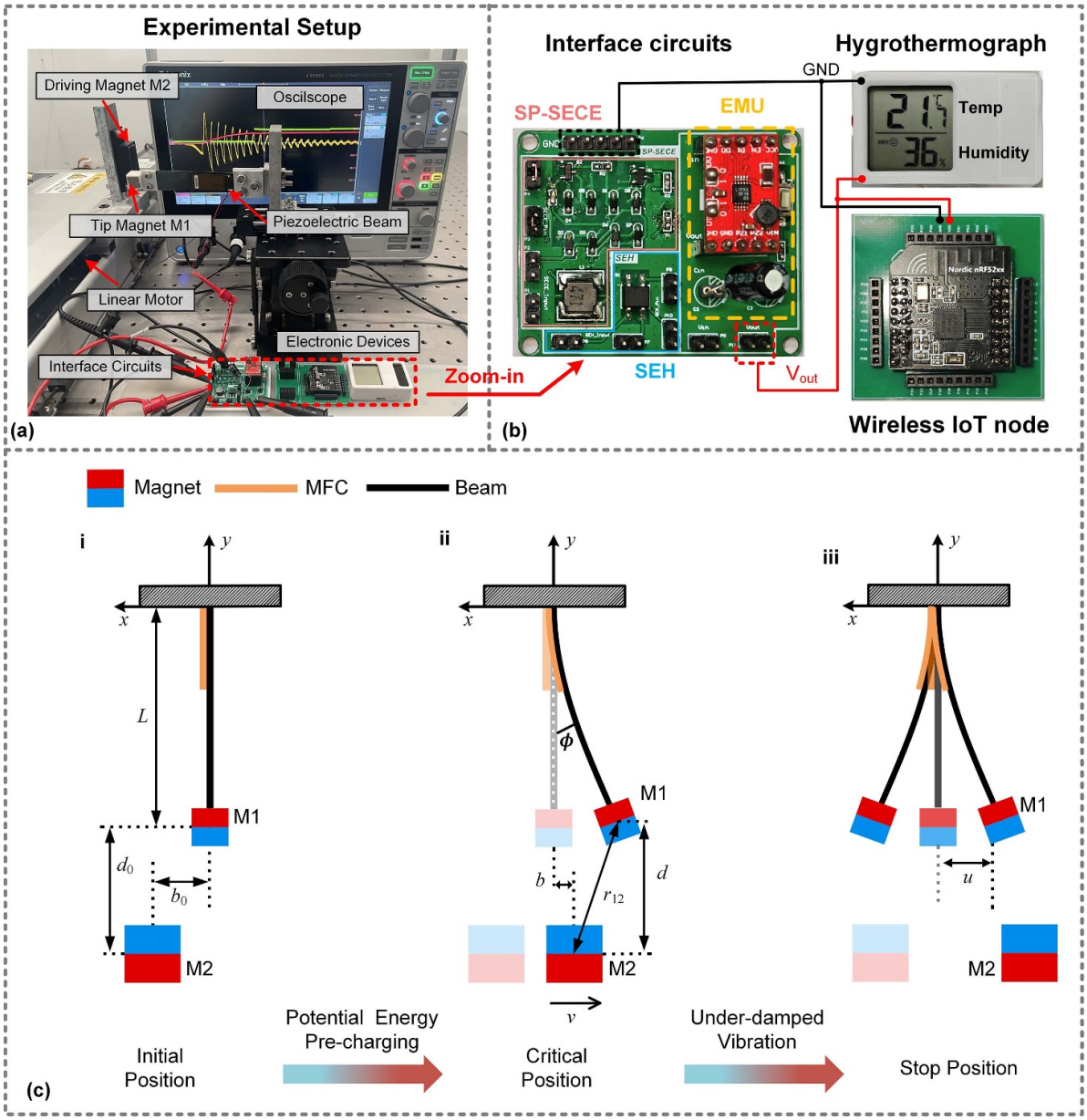

Figure 1. Experimental setup and system schematic (a) experimental setup of the TM-PEH, including a linear motor, piezoelectric beam, tip magnet (M1), driving magnet (M2), the interface circuits, the energy management unit, and electronic devices. (b) Layout of the interface circuits, energy management unit, and sensors: a hygrothermograph and a wireless IoT node. (c) Dynamic motion process of the TM-PEH: (i) initial position, (ii) critical position, and (iii) stop position.

Semiconductorn©, RF52832). An oscilloscope (Tektronix©, MDO34) was used to accurately capture the working waveforms in the experiments.

The dynamic process of the TM-PEH is elucidated in figure 1(c). A single plucking process can be divided into two distinct stages: the potential energy pre-charging stage and the energy-release stage. At the beginning of the first stage, the distance between the two magnets is too large to generate strong magnetic forces, and the piezoelectric beam remains unbent. At this moment, the total potential energy U_{total} stored in the beam is nearly zero. Subsequently, as the linear motor moves at a velocity of v, simulating the opening-door process, the magnetic repulsive force exerted on M1 by M2, which is mounted on the linear motor, increases, leading to the bending of the piezoelectric beam. In this process, the positive work done by M2 is gradually converted into the elastic potential energy U_{e} stored in the piezoelectric beam. When M2 reaches the critical position, the elastic potential energy stored in the piezoelectric beam reaches its maximum limit. As M2 further moves, the magnetic force applied on M1 can no longer counterbalance the restoring force of the piezoelectric beam. Therefore, the potential energy will be released and transformed into the kinetic energy of the beam, leading to its underdamped vibration. During the vibration, the mechanical

energy oscillates between potential and kinetic forms, and the piezoelectric transducer converts a portion of the mechanical energy into electricity.

According to many theories [36, 37], the TM-PEH can be represented as a lumped single-degree-of-freedom (SDOF) model, and the governing equations are formulated as follows:

$$\begin{cases} M\ddot{u} + D\dot{u} + Ku + \theta V_p = F_m(u,b) \\ I = \theta\dot{u} - C_p\dot{V}_p \end{cases} \tag{1}$$

where M represents the equivalent mass, K denotes the equivalent stiffness, and D stands for the damping coefficient. Additionally, V_p represents the voltage across the piezoelectric element, while I indicates the output current when the PEH is connected to a general load. C_p and θ denote the clamped capacitance and electromechanical coupling coefficient of the piezoelectric transducer, respectively. u represents the transverse displacement of the free end of the beam.

Based on the dipole–dipole interaction model [38], the magnetic force $F_m(u,b)$ exerted by M2 on M1 can be derived as:

$$F_m(u,b) = \frac{3\mu_0 m_1 m_2}{4\pi r_{12}^5}\left\{(u-b) + \frac{3\mathrm{d}u}{\sqrt{L^2-u^2}} - \frac{5d^2}{r_{12}^2}\left[(u-b) + \frac{\mathrm{d}u}{\sqrt{L^2-u^2}}\right]\right\} \tag{2}$$

where d indicates the longitudinal distance between the centers of the two magnets; ϕ is the angle of deflection, which corresponds to the angular displacement of the beam tip; r_{12} denotes the distance between M1 and M2 centers; m_1 and m_2 are the magnetic moments of M1 and M2, respectively; μ_0 denotes the vacuum permeability. Based on the geometric relationships, ϕ, d, and r_{12} can be formulated as follows,

$$\phi \approx \sin^{-1}(u/L) \tag{3}$$

$$d = d_0 + L(1-\cos\phi) \tag{4}$$

$$r_{12} = \sqrt{(u-b)^2 + d^2} \tag{5}$$

where L represents the distance from the fixed end of the piezoelectric beam to the center of M2, and d_0 denotes the initial longitudinal separation between the two magnets. b indicates the transverse distances between the centers of the two magnets. The intrinsic parameters for the experimental setup are listed in table 1.

Although the lumped SDOF model introduced above has been widely used, it is primarily suited for relatively simple loads. In practical scenarios, sophisticated loads, such as interface circuits incorporating transistors, introduce nonlinearities that substantially complicate, and in some cases preclude, analytical solutions to equation (1). To explore and analyze a more sophisticated electrical load, it is necessary to leverage the ECM approach for effective analysis. The fundamental principle of the ECM approach is grounded in mechanical-electrical analogies, established by identifying relationships between mechanical variables that exhibit a mathematical structure analogous to those in the electrical domain.

Table 1. Intrinsic parameters of the TM-PEH.

Description	Value
Length of beam L (mm)	86.5
Volume of Tip magnet M1 (mm^3)	1000
Volume of driving magnet M2 (mm^3)	6000
Magnetic constant μ_0 (H m^{-1})	$4\pi \times 10^{-7}$
Residual flux density of magnets B_r (T)	1.33

In the established ECM for the TM-PEH, the motion of the driving magnet M2 is emulated by a current source connected in parallel with a capacitor, while the magnetic force is modeled using an arbitrary behavioral voltage source that is governed by a custom control function. The mechanical domain is modeled using circuit components such as inductor L_m, resistor R_m, and capacitor C_m, which correspond to the equivalent mass, damping coefficient, and stiffness, respectively [39]. As for the electromechanical coupling term in equation (1), the piezoelectric transducer is modeled using a combination of arbitrary behavioral voltage and current sources. Once the mechanical structure and piezoelectric transducer are represented in this equivalent circuit framework, various electrical components, including interface circuits and EMUs, can be integrated for comprehensive system-level analysis.

To experimentally determine the equivalent circuit parameters, this study used an impedance measurement-based method [40, 41]. This approach enables the identification of the equivalent circuit parameters by analyzing the admittance spectrum obtained from an automated impedance analyzer. Figure 2(a) plots the experimentally obtained admittance spectrum using an impedance analyzer (Analog Discovery Impedance Analyzer). The slight asymmetry observed in the conductance curve can be attributed to the nonlinear behaviors of the fabricated PEH. Based on the measured data, the equivalent components L_m, R_m, C_m, and C_p were calculated. The electromechanical coupling coefficient θ was determined from the open-circuit voltage response under the harmonic excitation at a constant acceleration of 0.1 g. The identified parameters are summarized in table 2.

Figure 2(b) presents a comparison of the free-decay test responses of the piezoelectric cantilever beam, obtained from both experimental measurements and simulations utilizing the identified lumped parameters. The good agreement between the two results validates the parameter identification method.

3. Interface circuit analysis

Utilizing the ECM approach and identified parameters, we built an ECM incorporating the TM-PEH and the interface circuit, specifically the SEH and SP-SECE circuits. The SP-SECE circuit possesses both energy-boosting and load-independent characteristics, making it well-suited for weakly coupled piezoelectric energy harvesting systems in practical applications [42]. Since our system involves an EMU interfaced with nonlinear loads, the SP-SECE circuit was chosen

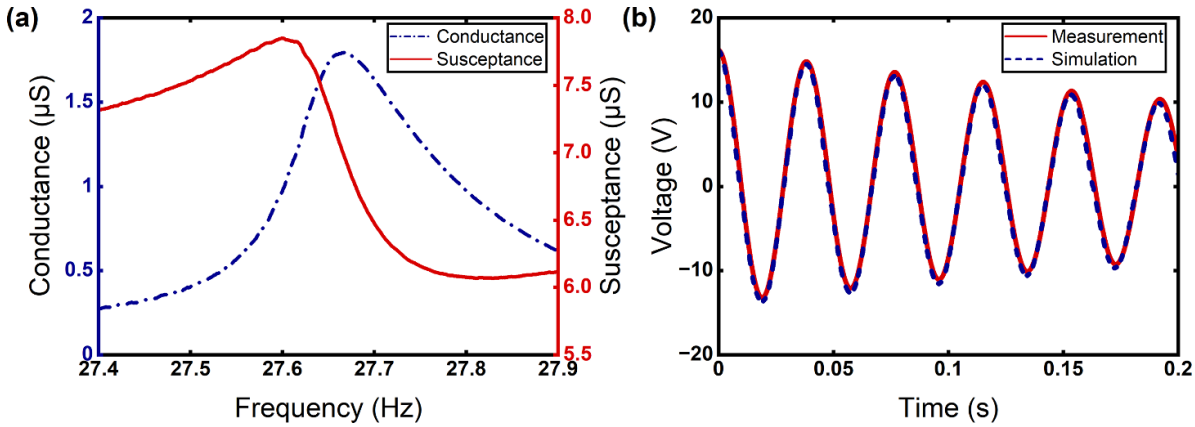

Figure 2. Impedance measurement-based parameter identification and model validation: (a) admittance spectrum of the TM-PEH and (b) comparison of simulated and experimental voltage responses in free decay oscillation.

Table 2. Experimentally identified equivalent parameters of the TM-PEH.

Description	Value
Equivalent mass of beam with tip magnet M1 M (g)	20.12
Equivalent damping coefficient D (Ns m^{-1})	0.14
Equivalent stiffness K (N m^{-1})	605.92
Clamped capacitance C_p (nF)	40.22
Electromechanical coefficient θ (N m^{-1})	0.000 6664
Dimensionless electromechanical coefficient k_m^2	0.0182

over other interface circuits, such as the SP-P-SSHI. The simulation was performed in LTspice, and experiments were carried out to validate the simulation results. The dimensionless coupling coefficient ${k_m}^2$ of the fabricated TM-PEH in this study was calculated to be 0.0182, as listed in table 2. According to previous studies [43, 44], this value classifies the system as weakly coupled.

Figure 3(a) compares the piezoelectric voltage waveforms of the SP-ECE circuit obtained from simulations and experimental measurements. In these cases, the initial longitudinal separation d_0 was set to 2.6 cm, and the transverse distance b, with an initial value of -0.1 m, varied as the linear motor moved at a constant velocity of 0.4 m s^{-1} . According to equation (2), the transverse distance could be expressed as $b = b_0 + 0.4\ t$ during the experiment. The simulation result matches well with the experimental one, effectively illustrating the main characteristics of the SP-SECE circuit: the voltage is flipped to zero once it reaches the peak due to the synchronized switching operation. Furthermore, figure 3(b) shows the charging performance of the SP-SECE circuit given different capacitances. The excellent agreement between the simulated and experimental data further substantiates the reliability of the ECM approach.

Based on the simulation model, we also investigated the advantages of the SP-SECE circuit compared to the SEH circuit in the application of charging capacitors. Six different capacitors, 22, 33, 47, 100, 220, and 330 μF, were used in the simulation. Figure 3(c) demonstrates that the SP-SECE circuit can always charge the capacitors to higher voltages. Figure 3(d) presents a direct comparison of the energy harvested in capacitors of different values. It is evident that the harvested energy by the SEH circuit drops sharply when charging larger storage capacitors, primarily due to the aggravated impedance mismatch. In contrast, the SP-SECE circuit exhibits a more gradual decline, consistent with the widely recognized load-independent nature attributed to its decoupled two-phase operation mechanism. The observed slight decrease for the SP-SECE circuit might result from the increased parasitic loss associated with the switching components [45]. In the simulation of charging a capacitor of 330 μF, the SP-SECE circuit collects nearly five times more energy, representing a remarkable 496% increase compared to the SEH circuit.

In addition to circuit simulation, the capacitor-charging tests of the SP-SECE and SEH circuits were performed experimentally. The results listed in table 3 confirm that the SP-SECE circuit consistently harvests more energy across all tested capacitors. For the 330 μF capacitor in the experimental test, the SP-SECE circuit harvested 411.62 μJ more energy than the SEH circuit, indicating an improvement of 468.12%, nearly fivefold. These results align well with the simulation findings, underscoring the effectiveness of the SP-SECE circuit in boosting efficiency and validating the accuracy of the ECM.

4. System-level simulation

In previous studies, the application of the equivalent circuit method was restricted to the analysis of interface circuits [31, 33], such as SECE and SSHI circuits. However, in addition to interface circuits, EMUs are crucial for practical applications, as different electronic devices often exhibit distinct power consumption characteristics. Prior studies did not consider these factors and failed to thoroughly analyze the operational dynamics of the whole system, comprising the PEH, interface circuit, EMU, and load device, from both mechanical and electrical perspectives. In this work, we extend the framework of ECM to incorporate EMUs and power consumption characteristics of load devices. Only through this approach can a comprehensive system-level simulation be

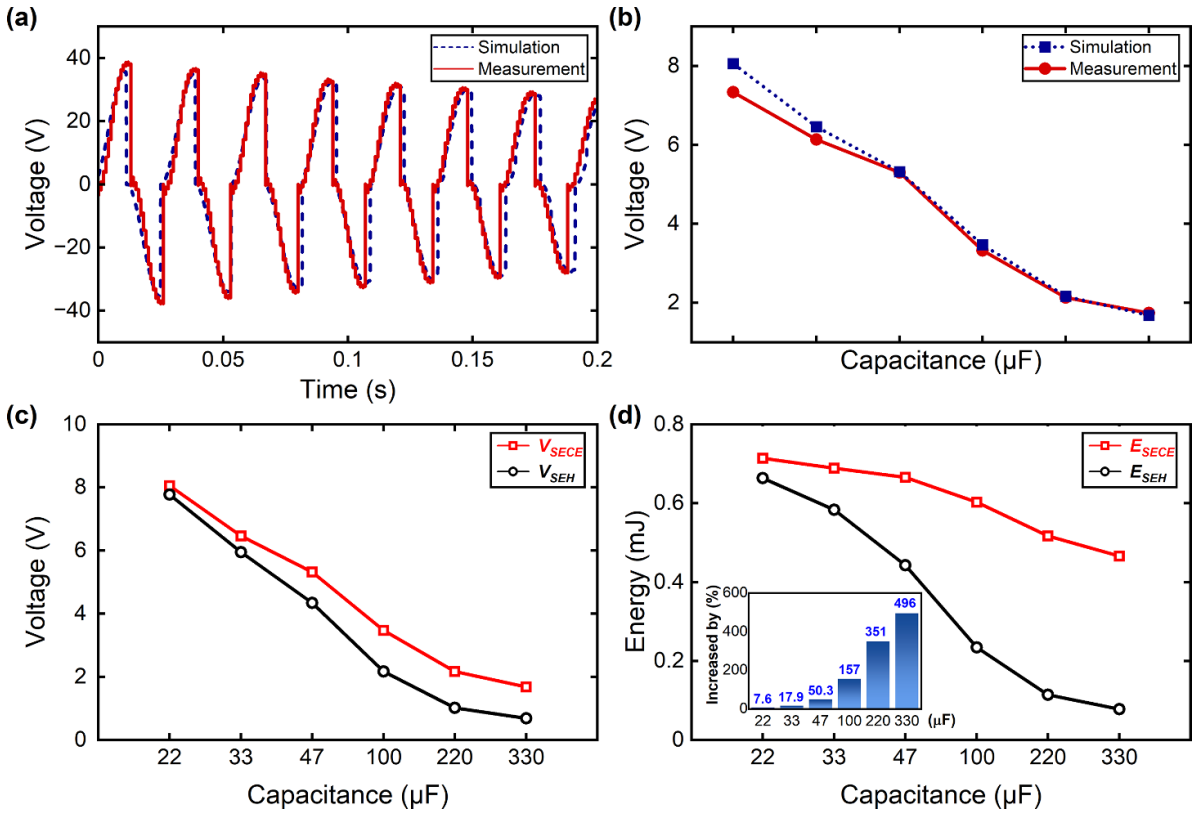

Figure 3. Simulation and experimental results for the TM-PEH shunted to interface circuits: (a) open-circuit voltage waveforms from simulation and experiments for the TM-PEH shunted to an SP-SECE circuit; (b) capacitor-charging performance of the SP-SECE circuit predicted by simulation and tested by experiments; (c) simulated comparison of charging voltages under varying capacitances for the SEH and SP-SECE circuits; (d) simulated comparison of charging energy for the SEH and SP-SECE circuits, including an inset showing the percentage increase in charging energy.

Table 3. Capacitor-charging performance of the SP-SECE and SEH circuits in the experiment.

	Charging voltage (V)		Charging energy (μJ)		
Capacitance (μF)	SP-SECE	SEH	SP-SECE	SEH	Increase
22	7.34	7.16	592.63	563.92	5.1%
33	6.13	5.68	620.02	532.33	16.47%
47	5.3	4.32	660.12	438.57	50.52%
100	3.33	2.01	554.45	202.01	174.47%
220	2.13	0.998	499.06	109.56	355.51%
330	1.74	0.73	499.55	87.93	468.12%

established, encompassing the entire process from energy harvesting to management and utilization. Figure 4 demonstrates the system-level ECM of the whole system, which includes the TM-PEH, the interface circuit, the EMU, and practical external loads. The electronic components used in the SP-SECE circuit are outlined in table 4.

The results presented in figure 3 and table 3 prove that the SP-SECE circuit exhibits greater efficiency than the SEH circuit in the simple capacitor-charging test. Through the system-level simulation, we further substantiate the advantages of the SP-SECE circuit in practical applications by comparing it with the SEH circuit in the application of powering a hygrothermograph and a wireless IoT node (Nrf52832) through a typical EMU, i.e. the LTC3588-1 module. In the experiment, we first used the current probe of the oscilloscope to characterize the distinct current consumption profiles of the two electronic devices. The hygrothermograph operates in a continuous mode, consistently monitoring the temperature and humidity. During operation, it draws a steady current of about 54.5 μA under a supply voltage of 1.8 V. Therefore, the hygrothermograph was directly emulated by a constant 33 KΩ resistor in the LTspice model, as illustrated in Part IV (Electronic Load 1). In contrast, the IoT node functions in an intermittent mode, activating periodically for 330 μs in each 1 s cycle, with a peak operational current measured of approximately 24.12 mA. To replicate this intermittent behavior, the IoT node was modeled using a time-varying resistor, controlled by a voltage-controlled switch that is driven by a pulse voltage source in LTspice simulation, as illustrated in Part IV (Electronic Load 2) of figure 5.

In both the experiment and simulation, we monitored and recorded the voltages at the input and output pins (V_{in} and V_{out}) of the LTC3588-1 module. Specifically, the input pin is connected to the storage capacitor of the SP-SECE circuit, while the output pin is directly used to power the applicable loads. Figure 5 demonstrates the simulation and experimental results of V_{in} and V_{out} under the conditions where the initial longitudinal separation was set $d_0 = 2.8$ cm, the initial transverse

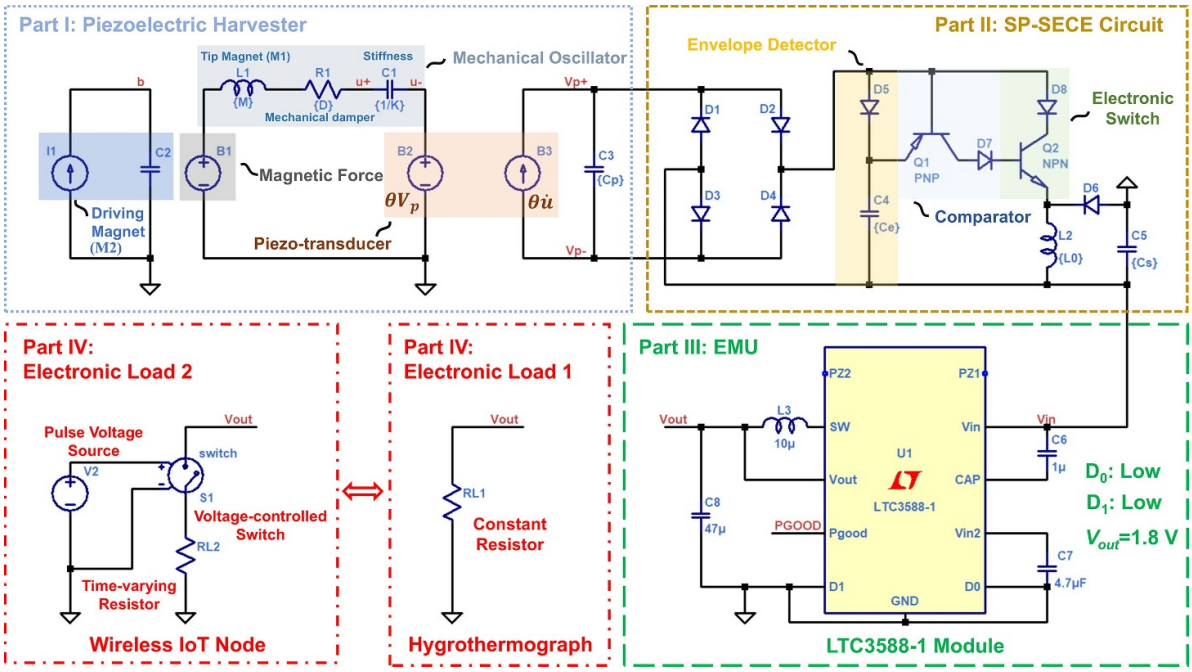

Figure 4. The schematic diagram of the system-level equivalent circuit model for the TM-PEH that is shunted to an SP-SECE circuit, regulated by an LTC3588-1 energy management unit, ultimately supplying power to a general electronic device.

Table 4. Component list of SP-SECE circuit.

Designator	Part number	Variable	Value
$D_{1–8}$	NSR02100HT1G	L_2	470 μH
Q_1(PNP)	MMBT5401	C_4	3 nF
Q_2(NPN)	MMBT5551	C_5	47 uF

distance was $b_0 = -0.1$ m, and the motor moved at a constant velocity of 0.4 m s^{-1} . Besides, the under voltage lockout (UVLO) settings of the LTC3588-1 module were configured with a minimum turn-on threshold voltage of 3.77 V, a turn-off threshold voltage of 2.87 V, and a stabilized voltage of 1.8 V while outputting. Figures 5(a) and (b) present the results of using the SP-SECE circuit to power the hygrothermograph. The simulation results are in excellent agreement with the experimental observations, where V_{in} rises beyond 3.77 V to a maximum value of around 4.51 V, thereby successfully triggering the UVLO function of the EMU and outputting a regulated 1.8 V V_{out}. Given the power generation capability of the TM-PEH and the SP-SECE circuit, the operation process of the whole system can be divided into three phases:

- Phase I—energy harvesting: during this phase, the energy harvested by the TM-PEH is regulated by the SP-SECE circuit and gradually charges the storage capacitor until the input voltage surpasses the turn-on threshold (3.77 V) of the LTC3588-1 module. This phase is characterized by a gradual voltage increase of V_{in}, as observed in both the simulation and experimental results.
- Phase II—sensor operation: once the output port of the LTC3588-1 module is activated, it delivers a stable voltage of 1.8 V to the hygrothermograph, which undergoes a cold start before entering its normal operating mode. In this mode, it monitors the ambient temperature and humidity, displaying the information on the screen. This phase lasts about 3 s, as depicted in figures 5(a) and (b).
- Phase III—power outage: after the electrical energy in the storage capacitor is depleted, V_{in} drops below the lockout threshold of the LTC3588-1 module, the power supply V_{out} is interrupted. Consequently, the hygrothermograph stops functioning due to an inadequate energy supply.

However, as shown in the subfigures in the second row, i.e. figures 5(c) and (d), when using the SEH circuit, the energy collected in the storage capacitor, indicated by V_{in}, can never reach the threshold 3.77 V. As a result, V_{out} remains zero under the control of the UVLO function of the LTC3588-1 module, and only Phase I were observed in this case.

The above hygrothermograph application demonstrates that the developed system-level simulation model effectively captures the power dynamics of the EMU and the electrical load in the TM-PEH system, which could not be analyzed in

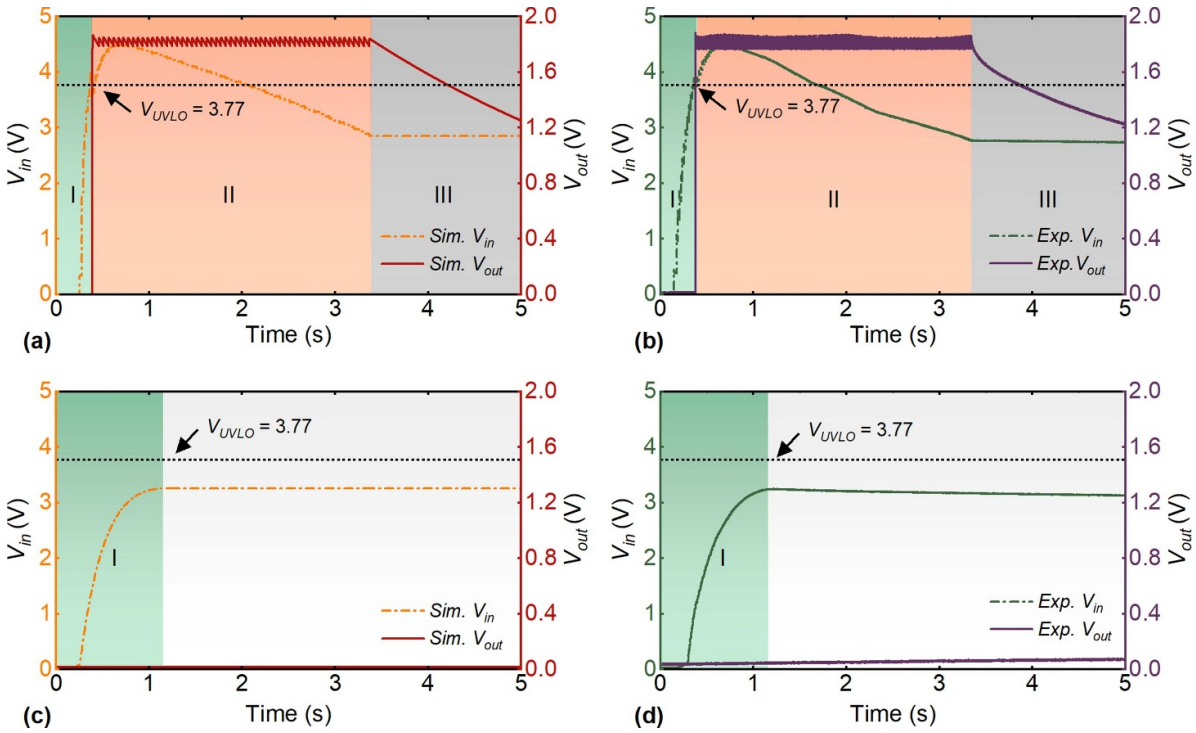

Figure 5. The simulation and experimental results for the TM-PEH powering the hygrothermograph via different interface circuits and the LTC3588-1 module: (a) simulation and (b) experimental results of input and output voltages of the LTC3588-1 module with the SP-SECE circuit; (c) simulation and (d) experimental results of input and output voltages of the LTC3588-1 module with the SEH circuit.

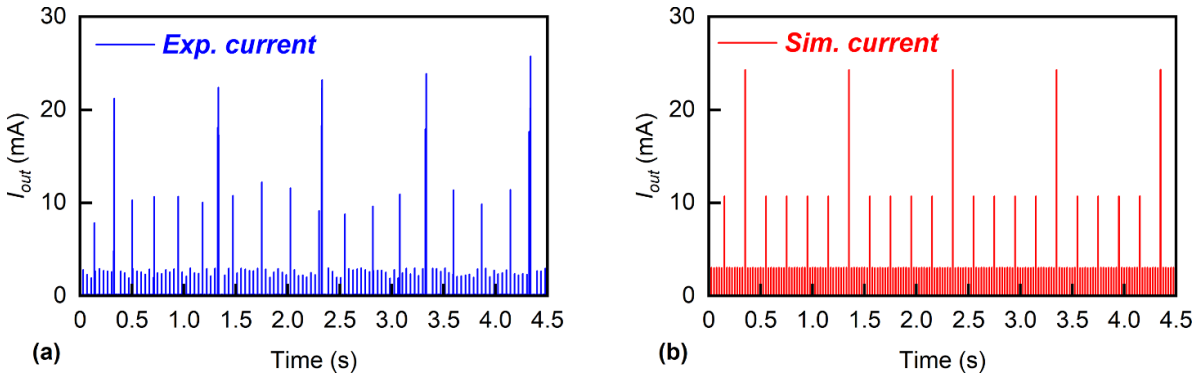

Figure 6. The operational current of the wireless IoT node operating in the intermittent mode. (a) experimental result; (b) simulation result.

previous studies. Notably, under the same excitation condition, the SEH fails to activate the hygrothermograph due to its limited energy harvesting efficiency, which stems from its inherent energy backflow issue [24]. In contrast, the SP-SECE circuit successfully powers the hygrothermograph for approximately 3 s, benefiting from its energy-boosting capability in a weak electromechanical coupling system [46, 47]. This result demonstrates that the system-level simulation facilitates efficient design, evaluation, and optimization of self-powered sensing/monitoring systems directly on a laptop, thereby reducing reliance on costly and time-consuming trial-and-error experiments in the laboratory.

The hygrothermograph operates in continuous mode, which is reflected by the gradual and smooth decline of the input voltage shown in figures 5(a) and (b), indicating a steady power consumption. In many other practical applications, we may have electronic devices working in intermittent modes. To further showcase the effectiveness and versatility of the developed system-level ECM, a wireless IoT node operating in intermittent mode was tested. First, its operational current was measured under a DC power supply with an output voltage of 3.6 V. As shown in figure 6(a), the results indicate that an advertisement packet is transmitted every 1 s, during which the power consumption significantly increases. Between transmission events, the IoT node enters standby mode, drawing a relatively low current. In LTspice, the periodically varying power consumption was emulated using a time-varying resistor with the value defined through conditional statements

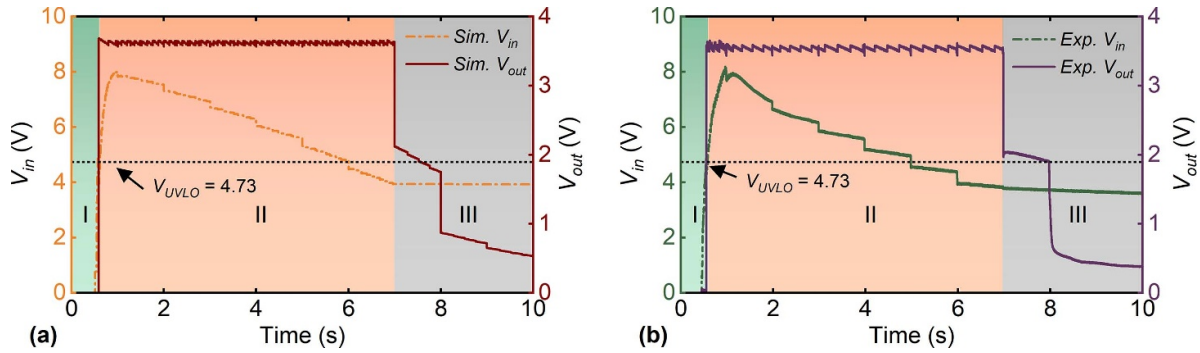

Figure 7. The simulation and experimental results for the TM-PEH powering the hygrothermograph via the SP-SECE circuit and the LTC3588-1 module: (a) simulation and (b) experimental results of input and output voltages of the LTC3588-1 module.

to replicate the experimentally identified power consumption profile. A pulse voltage source, in combination with a voltage-controlled switch, was utilized to alternate between the transmission and standby states. The corresponding simulation setup is detailed in Part IV (Electronic Load 2) of figure 5, and the simulated operational current is shown in figure 6(b).

Given that the SP-SECE has already demonstrated superior efficiency, only the SP-SECE circuit was utilized in the second case study to eliminate redundancy. Figures 7(a) and (b) illustrate the time-history voltage responses of V_{in} and V_{out} obtained from the simulation and experiment. In this case, the turn-on and turn-off threshold voltages of the LTC3588-1 unit were 4.73 V and 3.75 V, respectively, with a regulated voltage output of 3.6 V. Additionally, the initial longitudinal separation d_0 was reduced to 2.4 cm to enhance the energy input from the magnetic force. The results show that the value of V_{in} gradually increases, and once it exceeds the 4.73 V turn-on threshold, the UVLO function of the LTC3588-1 module is triggered, a stabilized voltage of 3.6 V is supplied to the IoT node, which transmits advertisement packets every 1 s. The good agreement between the two datasets confirms the reliability and accuracy of the system-level ECM. Notably, the improved ECM can accurately predict the activation timing of the wireless IoT node, benefiting from the refined modeling of the TM-PEH, interface circuit, EMU, and power characteristics of the electronic device. In addition, it exquisitely reveals the periodic energy consumption pattern of the IoT node during operation: the voltage decline is more stairwise rather than smooth. The interval between the two voltage drops is 1 s, coinciding perfectly with the advertisement interval of the IoT node. Slight discrepancies between the simulation and experimental results are observed, especially in the last phase. These discrepancies might arise from several factors, including variations between the actual electronic components and those used in the simulation software, as well as inaccuracies in identifying the power characteristics of the IoT node.

Overall, the above two case studies have well-validated the extended framework for system-level simulation of self-powered systems, accounting for mechanical dynamics, piezoelectric transducers, interface circuits, energy management modules, and external loads exhibiting complex dynamic behaviors, including intermittent modes. Future work will focus on extending the framework to incorporate more complex mechanical structures and electronic devices, thereby enhancing its applicability and robustness in practical scenarios.

5. Conclusion

In conclusion, this paper has presented an extended framework for building ECMs of self-powered systems. Within this framework, we have studied a TM-driven PEH (TM-PEH). Regarding the interface circuit, we examined a SEH circuit and a SP-SECE circuit. Both simulation and experimental results indicated that the SP-SECE circuit showcased a higher energy harvesting efficiency, especially for larger storage capacitors. Given the TM-PEH under the same excitation conditions, the SP-SECE circuit could harvest almost five times more energy than the SEH circuit in charging a 330 μF capacitor.

Unlike previous studies limited to the analysis of interface circuits, we further extended the simulation model to incorporate an EMU and two electronic devices (a hygrothermograph and a wireless IoT node) into consideration. The hygrothermograph was represented by a constant resistor in the simulation model, as it worked in continuous mode. In contrast, the wireless IoT node operated in intermittent mode. The periodic behavior was emulated by using a time-varying resistor, a pulse voltage source, and a voltage-controlled switch in LTspice. With elaborately designed load settings, the simulations enable us to differentiate between the two operational modes. Similar to the experimental observation, the simulated voltage response of the IoT node powered by the TM-PEH exhibits a periodic energy consumption pattern during operation. Moreover, the system-level simulations can accurately capture the operational dynamics of the whole system, especially the power dynamics of the EMU and practical

load devices. The methodology and results presented in this paper provide valuable insights and guidelines for designing self-sustained systems utilizing energy harvesting technology from a holistic perspective, considering the synergy of cross-disciplinary knowledge.

Data availability statement

All data that support the findings of this study are included within the article (and any supplementary files).

Acknowledgments

This work was supported by the National Natural Science Foundation of China (Grant No. 52305135), the Guangdong Provincial Key Lab of Integrated Communication, Sensing and Computation for Ubiquitous Internet of Things (Grant No.2023B1212010007), the Guangzhou Municipal Science and Technology Project (Grant No. 2023A03J0011), and the Guangzhou Municipal Key Laboratory on Future Networked Systems (Grant No. 024A03J0623).

ORCID iD

Guobiao Hu https://orcid.org/0000-0002-1288-7564

References

[1] Zanella A, Bui N, Castellani A, Vangelista L and Zorzi M 2014 Internet of things for smart cities *IEEE Internet Things J.* **1** 22–32
[2] Lampropoulos G, Siakas K and Anastasiadis T 2019 Internet of things in the context of industry 4.0: an overview *Int. J. Entrep. Knowl.* **7** 4–19
[3] Zeadally S, Shaikh F K, Talpur A and Sheng Q Z 2020 Design architectures for energy harvesting in the internet of things *Renew. Sustain. Energy Rev.* **128** 109901
[4] Sanislav T, Mois G D, Zeadally S and Folea S C 2021 Energy harvesting techniques for Internet of Things (IoT) *IEEE Access* **9** 39530–49
[5] Zhou S, Lallart M and Erturk A 2022 Multistable vibration energy harvesters: principle, progress, and perspectives *J. Sound Vib.* **528** 116886
[6] Hu G, Tang L, Liang J, Lan C and Das R 2021 Acoustic-elastic metamaterials and phononic crystals for energy harvesting: a review *Smart Mater. Struct.* **30** 085025
[7] Hu G, Liang J, Lan C and Tang L 2020 A twist piezoelectric beam for multi-directional energy harvesting *Smart Mater. Struct.* **29** 11LT01
[8] Zhang Y, Luo A, Wang Y, Dai X, Lu Y and Wang F 2020 Rotational electromagnetic energy harvester for human motion application at low frequency *Appl. Phys. Lett.* **116** 053902
[9] Wang Y *et al* 2024 A rolling-mode triboelectric nanogenerator with multi-tunnel grating electrodes and opposite-charge-enhancement for wave energy harvesting *Nat. Commun.* **15** 6834
[10] Sezer N and Koç M 2021 A comprehensive review on the state-of-the-art of piezoelectric energy harvesting *Nano Energy* **80** 105567
[11] Erturk A and Inman D J 2008 A distributed parameter electromechanical model for cantilevered piezoelectric energy harvesters *J. Vib. Acoust.* **130** 041002
[12] Lan C, Chen Z, Hu G, Liao Y and Qin W 2021 Achieve frequency-self-tracking energy harvesting using a passively adaptive cantilever beam *Mech. Syst. Signal Process.* **156** 107672
[13] Qian F, Hajj M R and Zuo L 2020 Bio-inspired bi-stable piezoelectric harvester for broadband vibration energy harvesting *Energy Convers. Manage.* **222** 113174
[14] Erturk A, Hoffmann J and Inman D J 2009 A piezomagnetoelastic structure for broadband vibration energy harvesting *Appl. Phys. Lett.* **94** 254102
[15] Huang Y, Hu G, Zhao C, Tang B, Mu X and Yang Y 2023 An L-shaped and bending-torsion coupled beam for self-adaptive vibration energy harvesting *J. Appl. Phys.* **56** 284001
[16] Li Z, Peng X, Hu G and Peng Y 2022 Theoretical, numerical, and experimental studies of a frequency up-conversion piezoelectric energy harvester *Int. J. Mech. Sci.* **223** 107299
[17] Li X, Chuai X, Hu G, Zhang D, Cai M, Wang C, Yang Y, Liao W-H and Liang J 2024 Energy and dynamics analysis of a single plucking energy harvester for transient-motion-powered IoT applications *Energy Convers. Manage.* **310** 118465
[18] He L, Liu L, Zhou J, Yu G, Sun B and Cheng G 2022 Design and analysis of a double-acting nonlinear wideband piezoelectric energy harvester under plucking and collision *Energy* **239** 122370
[19] Fu H and Yeatman E M 2018 Effective piezoelectric energy harvesting using beam plucking and a synchronized switch harvesting circuit *Smart Mater. Struct.* **27** 084003
[20] Ahmad M M, Khan N M and Khan F U 2021 Review of frequency up-conversion vibration energy harvesters using impact and plucking mechanism *Int. J. Energy Res.* **45** 15609–45
[21] Lefeuvre E, Badel A, Brenes A, Seok S, Woytasik M and Yoo C-S 2017 Analysis of piezoelectric energy harvesting system with tunable SECE interface *Smart Mater. Struct.* **26** 035065
[22] Tian W, Zhao Z, Liu W, Zhu Q, Zhang Z and Yuan Y 2021 Analysis on the power and bandwidth improvement of a frequency-tuning optimized SECE circuit *Sens. Actuators A* **332** 113110
[23] Badel A and Lefeuvre E 2016 *Nonlinear Conditioning Circuits for Piezoelectric Energy Harvesters. Nonlinearity in Energy Harvesting Systems* ed E Blokhina, A E Aroudi, E Alarcon and D Galayko (Springer) pp 321–59
[24] Liang J and Liao W-H 2011 Energy flow in piezoelectric energy harvesting systems *Smart Mater. Struct.* **20** 015005
[25] Lefeuvre E, Badel A, Richard C and Guyomar D 2005 Piezoelectric energy harvesting device optimization by synchronous electric charge extraction *J. Intell. Mater. Syst. Struct.* **16** 865–76
[26] Wu Y, Badel A, Formosa F, Liu W and Agbossou A E 2013 Piezoelectric vibration energy harvesting by optimized synchronous electric charge extraction *J. Intell. Mater. Syst. Struct.* **24** 1445–58
[27] Guyomar D, Badel A, Lefeuvre E and Richard C 2005 Toward energy harvesting using active materials and conversion improvement by nonlinear processing *IEEE Trans. Ultrason. Ferroelectr. Freq. Control.* **52** 584–95
[28] Lefeuvre E, Badel A, Richard C, Petit L and Guyomar D 2006 A comparison between several vibration-powered piezoelectric generators for standalone systems *Sens. Actuators A* **126** 405–16

[29] Yang Y and Tang L 2009 Equivalent circuit modeling of piezoelectric energy harvesters *J. Intell. Mater. Syst. Struct.* **20** 2223–35
[30] Bayik B, Aghakhani A, Basdogan I and Erturk A 2016 Equivalent circuit modeling of a piezo-patch energy harvester on a thin plate with AC–DC conversion *Smart Mater. Struct.* **25** 055015
[31] Wang J, Luo L, Yurchenko D and Hu G 2025 Equivalent circuit analysis of a nonlinear vortex-induced vibration piezoelectric energy harvester using synchronized switch technique *IEEE Trans. Ind. Electron.* **72** 4865–76
[32] Tang L, Zhao L, Yang Y and Lefeuvre E 2015 Equivalent circuit representation and analysis of galloping-based wind energy harvesting *IEEE/ASME Trans. Mechatronics* **20** 834–44
[33] Jia J, Shan X, Zhang X, Xie T and Yang Y 2022 Equivalent circuit modeling and analysis of aerodynamic vortex-induced piezoelectric energy harvesting *Smart Mater. Struct.* **31** 035009
[34] Li X, Tang H, Hu G, Zhao B and Liang J 2022 ViPSN-pluck: a transient-motion-powered motion detector *IEEE Internet Things J.* **9** 3372–82
[35] Li X, Teng L, Tang H, Chen J, Wang H, Liu Y, Fu M and Liang J 2021 ViPSN: a vibration-powered IoT platform *IEEE Internet Things J.* **8** 1728–39
[36] Erturk A and Inman D J 2008 On mechanical modeling of cantilevered piezoelectric vibration energy harvesters *J. Intell. Mater. Syst. Struct.* **19** 1311–25
[37] Hu G, Wang J and Tang L 2021 A comb-like beam based piezoelectric system for galloping energy harvesting *Mech. Syst. Signal Process.* **150** 107301
[38] Lan C, Tang L, Qin W and Xiong L 2018 Magnetically coupled dual-beam energy harvester: benefit and trade-off *J. Intell. Mater. Syst. Struct.* **29** 1216–35
[39] Wang J, Tang L, Zhao L, Hu G, Song R and Xu K 2020 Equivalent circuit representation of a vortex-induced vibration-based energy harvester using a semi-empirical lumped parameter approach *Int. J. Energy Res.* **44** 4516–28
[40] Hoseyni S M, Aghakhani A and Basdogan I 2024 Experimental admittance-based system identification for equivalent circuit modeling of piezoelectric energy harvesters on a plate *Mech. Syst. Signal Process.* **208** 111016
[41] Kuang Y, Chew Z J and Zhu M 2020 Strongly coupled piezoelectric energy harvesters: finite element modelling and experimental validation *Energy Convers. Manage.* **213** 112855
[42] Wu Y, Badel A, Formosa F, Liu W and Agbossou A 2014 Self-powered optimized synchronous electric charge extraction circuit for piezoelectric energy harvesting *J. Intell. Mater. Syst. Struct.* **25** 2165–76
[43] Liao Y and Liang J 2018 Maximum power, optimal load, and impedance analysis of piezoelectric vibration energy harvesters *Smart Mater. Struct.* **27** 075053
[44] Brenes A, Morel A, Gibus D, Yoo C-S, Gasnier P, Lefeuvre E and Badel A 2020 Large-bandwidth piezoelectric energy harvesting with frequency-tuning synchronized electric charge extraction *Sens. Actuators A* **302** 111759
[45] Tang H, Liu W, Hu G, Liu J and Dong D 2025 Optimized multi-step synchronous electric charge extraction via accurate electrical efficiency analysis *Smart Mater. Struct.* **34** 025027
[46] Brenes A, Morel A, Juillard J, Lefeuvre E and Badel A 2020 Maximum power point of piezoelectric energy harvesters: a review of optimality condition for electrical tuning *Smart Mater. Struct.* **29** 033001
[47] Morel A, Brenes A, Gibus D, Lefeuvre E, Gasnier P, Pillonnet G and Badel A 2022 A comparative study of electrical interfaces for tunable piezoelectric vibration energy harvesting *Smart Mater. Struct.* **31** 045016